Volume 49
Number 31
21 August 2020
Pages 10665-11030

Dalton Transactions

An international journal of inorganic chemistry

rsc.li/dalton

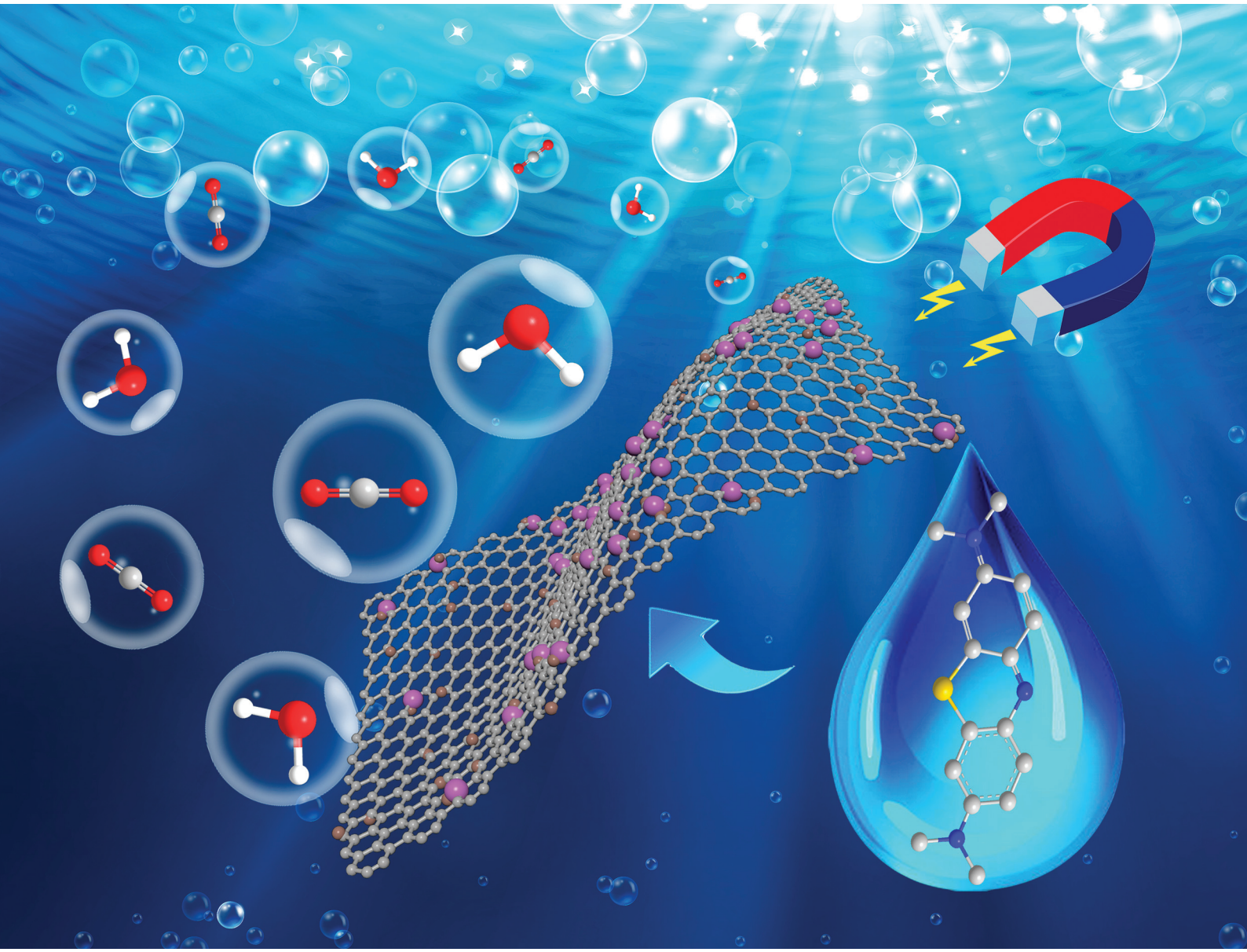

ISSN 1477-9226

ROYAL SOCIETY OF CHEMISTRY

PAPER

Sisi Feng, Miaoli Zhu, Shengqian Ma *et al.*
The first ternary Nd-MOF/GO/Fe_3O_4 nanocomposite exhibiting an excellent photocatalytic performance for dye degradation

Dalton Transactions

ROYAL SOCIETY OF CHEMISTRY

PAPER

View Article Online
View Journal | View Issue

Cite this: *Dalton Trans.*, 2020, **49**, 10745

The first ternary Nd-MOF/GO/Fe_3O_4 nanocomposite exhibiting an excellent photocatalytic performance for dye degradation†

Yuting Bai,[a] Shuo Zhang,[a] Sisi Feng,*[b,c] Miaoli Zhu*[a,b] and Shengqian Ma*[c]

Received 6th May 2020,
Accepted 2nd June 2020

DOI: 10.1039/d0dt01648a

rsc.li/dalton

Herein, a ternary nanocomposite photocatalyst (**MOF-1**/GO/Fe_3O_4) based on a novel Nd-MOF, graphene oxide (GO), and Fe_3O_4 was successfully prepared. It was verified that the MOF nanoparticles and GO sheets were integrated by means of intimate interfacial contacts and a large number of Fe_3O_4 microspheres were uniformly loaded on the surface of GO. The ternary nanocomposite was a stable, environmentally friendly, and efficient visible-light photocatalyst, which displayed excellent photocatalytic performance in the degradation of methylene blue (MB) (~95%) dye within 80 min under sunlight irradiation in the aqueous solution. Compared to **MOF-1**, the photocatalytic efficiency of the composite was improved by 90% and the excitation wavelength was moved from the ultraviolet to visible region. The enhancement of photocatalytic performance can be ascribed to the introduction of GO, which efficiently accelerated electron migration, minimized the recombination of photogenerated electron–hole pairs, and improved the optical absorption properties, leading to a synergistic facilitation of the photocatalysis process. The ternary composite demonstrated excellent stability and reusability and can be easily recovered by a magnetic field. The study would provide novel avenues for the preparation of highly efficient and environmentally stable photocatalysts for organic wastewater treatment.

Introduction

Wastewater from textile, chemical, paper, and food industries has a significant impact on human health, which has attracted a considerable amount of attention from a number of researchers in recent years.[1] Organic dyes are the most common contaminants in wastewater because they consume the dissolved oxygen that inhibits light penetration and thus affect aquatic plants, causing severe impact on the ecosystem.[2] It is therefore urgently imperative to quest for effective solutions to alleviate water pollution. Many approaches for the treatment of sewage such as physical adsorption, photo-Fenton oxidations, advanced oxidation processes, and photocatalytic degradation have been reported in the literature. Among these, photocatalytic degradation has been recognized as a powerful technology for water treatment until nowadays due to its benign nature and low cost.[3,4]

Recently, metal–organic frameworks (MOFs) appealed as burgeoning materials for environmental remediation have aroused more attention in the field of photocatalysis.[5,6] Compared with the conventional photocatalysts, MOF materials have more advantages in improving the photocatalytic effect as their desirable topology and high surface area allow not only for rapid transportation but also for the good accommodation of guest molecules.[7] To date, the photocatalytic properties of some MOFs have been studied and the application of MOFs as potential photocatalysts has been proved. For instance, Garcia and his team demonstrated that MOF-5 could perform as a semiconductor and displayed its photocatalytic activity in certain reactions.[8] MIL-88A was synthesized as a photocatalyst for the degradation of Orange G.[9] The excellent activity of MOF 235 in the degradation of RhB under visible light was also investigated.[10]

However, despite the MOFs having photocatalytic properties, the activity of MOF photocatalysts is immensely limited by the fast recombination rate of the photogenerated electron–hole pairs; hence, they cannot meet the needs for

[a]*Institute of Molecular Science, Key Laboratory of Chemical Biology and Molecular Engineering of the Education Ministry, Shanxi University, Taiyuan, Shanxi 030006, P. R. China. E-mail: miaoli@sxu.edu.cn*
[b]*Key Laboratory of Materials for Energy Conversion and Storage of Shanxi Province; Shanxi University, Taiyuan, Shanxi, 030006, P. R. China. E-mail: ssfeng@sxu.edu.cn*
[c]*Department of Chemistry, University of South Florida, 4202 Easter Fowler Avenue, Tampa, Florida 33620, USA. E-mail: sqma@usf.edu*

†Electronic supplementary information (ESI) available: Crystal details, N_2 adsorption–desorption isotherms UV, PXRD, IR, ICP and LC-MS. CCDC 1962617. For ESI and crystallographic data in CIF or other electronic format see DOI: 10.1039/D0DT01648A

practical applications.[11] Thus, it is desired to find some simple and direct approaches for improving the photocatalytic performance of MOFs.[12,13] Among them, one of the most effective techniques is the use of graphene oxide (GO) supported MOF composite materials as heterojunction photocatalysts for the conversion of solar light into chemical energy. GO formed from the oxidation of graphite is one of the most ideal candidates for the separation and transfer of photogenerated carriers owing to its large specific surface area, excellent thermal and chemical stability, and outstanding mobility of the charge carriers.[14,15] There is a great deal of oxygen-containing functional groups such as –CO–, –OH, and –CH(O)CH– on the surface of GO, which facilitate the coordination of GO with the metal center of MOFs; hence, the crystal grows onto the graphene layer.[16,17] We can maximize the electron transport performance of GO, and thus, improve the photocatalytic activity of MOFs, which can be attributed to the interfacial contacts between GO and MOFs. Currently, the process has been used to synthesize a variety of GO-based nanocomposites, which exhibit superior adsorption and photocatalytic properties. In the past few decades, scientists have prepared numerous graphene-based MOF photocatalysts.[18–20] However, the major issue in the practical application of photocatalysis system is the complicated separation of photocatalysts from the reaction medium after photodegradation owing to the good dispersive properties of these photocatalysts. To address this problem, photocatalysts that can be recovered under an external magnetic field has been proposed as a possible solution.[21] Fe_3O_4 was selected as a superparamagnetic material because of its excellent magnetic properties, low cost, high abundance, environmental benignity, simple preparation methods, and strong super-paramagnetic properties. Although there have been some reports on the use of MOF/GO and MOF/Fe_3O_4 nanocomposites[22–25] as photocatalysts, to the best of our knowledge, the research works focused on the preparation of the MOF/GO/Fe_3O_4 composite as photocatalysts that have the advantages of GO and magnetic field responsive separation simultaneously are rather scarce.

In this work, we designed a novel Nd-MOF (**MOF-1**) as the component because its intervalence electron can be transferred by ultraviolet light and its neodymium ion has stable different valence states. This is the first photocatalyst based on the Nd-MOF for the degradation of dyes. In particular, this material combined with GO and Fe_3O_4, the ternary composite showed an excellent specific photocatalytic degradation property in the aqueous solution with outstanding stability and reusability. The absorption spectrum can also be moved to the visible region. It is exciting that the photocatalytic efficiency of the **MOF-1**/GO/Fe_3O_4 nanocomposite toward methylene blue (MB) degradation in aqueous solution was increased by 90% than that of their single-component materials. This improvement of the photocatalytic performance was found to be closely dependent on the addition of GO that efficiently promoted the separation of charge carriers and increased the optical absorption properties. Besides, the **MOF-1**/GO/Fe_3O_4 nanocomposites could be recovered and reused from the treated water through an external magnetic field. Therefore, **MOF-1**/GO/Fe_3O_4 nanocomposite is an important candidate for the decolorization of organic contaminants in wastewater under visible light because of its convenient preparation, outstanding photocatalytic activity, and high stability.

Experimental

Materials

1,3,5-Tris(4-carbon(phenoxy)benzene) (H_3TCPB) was purchased from the Jinan Camolai Trading Company, China. Graphene oxide (GO) was prepared according to the methods in the literature.[26] All reagents and solvents were used without any further purification. The FT-IR spectra were recorded on a BRUKER TENSOR27 spectrometer with KBr disks. The powder X-ray diffraction patterns (PXRD) were recorded using a Bruker D8 Advance X-ray diffractometer employing Cu-Kα radiation with a 2θ value ranging from 5° to 60°. The thermogravimetric analysis (TGA) was performed by using a DuPont thermal analyser from 2 °C to 800 °C with a heating rate of 10 K min^{-1} and under a N_2 atmosphere. UV-vis diffuse reflectance spectroscopy (DRS) was performed by using a TU-1950 UV-vis spectrophotometer, during which $BaSO_4$ was adopted as the internal reflectivity standard. The morphology was observed on a JSM-7001F field emission scanning electron microscope (FE-SEM). The BET surface area and porous property were measured by using a Micromeritics ASAP 2020 analyzer. The concentration of iron ions in the suspension was detected by inductively coupled plasma mass spectrometry (ICP-MS) (NexION350X). The electrochemical impedance spectroscopy (EIS) was performed under a status of open-circuit voltage and over the frequency range of 100 kHz to 0.01 Hz. The liquid chromatography-mass spectrometry (LC-MS) analysis was performed by using a Thermo Scientific Q Exactive. The Mott–Schottky analysis was performed on an electrochemical workstation (RST5200F). The UV/visible spectra were recorded with a JASCO V-570 spectrophotometer.

Synthetic procedures

Preparation of $[Nd_2(TCPB)_2(DMF)(H_2O)]_n$ (MOF-1 or 1). A mixture of $NdCl_3{\cdot}6H_2O$ (35.9 mg, 0.1 mmol), H_3TCPB (48.6 mg, 0.1 mmol), distilled water (2.0 mL), C_2H_5OH (3.0 mL), and *N*,*N*-dimethylformamide (DMF) (3.0 mL) was stirred for 30 min and transferred into a stainless steel autoclave with a Teflon liner (23.0 mL). After a hydrothermal process under autogenous pressure at 393 K for 72 h, the reactor was naturally cooled to RT. The purple bulk crystals were collected by filtration, washed with H_2O, and dried in air, obtaining a yield of ~42% based on H_3TCPB. Analysis calculated for $C_{57}H_{39}NO_{20}Nd_2$: C 50.80, H 2.89, N 1.04; found: C 49.98, H 2.98, N 1.65. IR (KBr, ν/cm^{-1}; s = strong, m = medium, and w = weak): 3414m, 1927w, 1651s, 1597s, 1533s, 1503s, 1454m, 1410s, 1348m, 1232s, 1168s, 1113w, 1010w, 784s, 712m, 623w, and 437w (Fig. 2b).

X-ray crystallography and structure solution. Crystallographic data for $[Nd_2(TCPB)_2(DMF)(H_2O)]_n$ was collected by using a CrysAlisPro, Agilent Technologies with a SuperNova, Dual, Cu at zero, Eos with Cu-Kα (λ = 1.5418 Å) as the radiation source. The structure was obtained by direct methods and refined by full-matrix least-square methods on F^2 using the SHELXTL-2018.[27] All the non-H atoms were refined anisotropically. In the processes of refinements for **MOF-1**, solvent DMF molecules and H_2O molecules were found to be severely disordered and were refined with some occupancies from the diffraction data and the reports of element analyses. Seriously disordered atoms and relevant distances were constrained by ISOR and DFIX instructions. The attempt to locate H atoms to the disordered H_2O molecules of **MOF-1** was unsuccessful. Therefore, the H atoms of some disordered O atoms belong to an unknown or inconsistent label in CHECKCIF, but their contributions were also included in the overall formula. The topological analyses were performed using the Topos Pro program. The crystallographic data, the data collection, and refinement parameters of **MOF-1** are provided in Table 1. Crystallographic data in CIF format is deposited with the Cambridge Crystallographic Data Center as CCDC 1962617† for **MOF-1**. The selected bond lengths, Nd···Nd distances, and angles of **MOF-1** are listed in Table S1.†

Preparation of MOF-1/GO/Fe_3O_4. Fe_3O_4 nanoparticles were synthesized following the most commonly used method.[28] **MOF-1** was first dispersed in ethanol by stirring until the mixture turned into a homogeneous solution. Next, GO with the desired weight was dispersed in 10.0 mL of ethanol, sonicated for 15 min, and then added the above dispersions into a flask. After reflux for 4 hours, **MOF-1**/GO could be obtained *via* rotating evaporation. Finally, the **MOF-1**/GO/Fe_3O_4 nanocomposite was obtained by adding quantitative Fe_3O_4 and **MOF-1**/GO in ethanol that was well dissolved through ultrasonic vibration. The corresponding **MOF-1**/GO/Fe_3O_4 composites were labelled as **MOF-1**/GO/Fe_3O_4-*x*, where *x* (wt%) refers to the mass fraction of GO in the composites. **MOF-1**/GO/Fe_3O_4-5–**MOF-1**/GO/Fe_3O_4-22 were prepared in this work. Among all the samples synthesized, the **MOF-1**/GO/Fe_3O_4-9 was found to have the best photocatalytic performance. Thus, **MOF-1**/GO/Fe_3O_4 in this study refers to the **MOF-1**/GO/Fe_3O_4-9 nanocomposite without further labelling.

Photocatalytic activity measurements. To evaluate the photocatalytic behavior of the **MOF-1**/GO/Fe_3O_4 nanocomposite, the degradation of MB aqueous solution (10 mg L^{-1}) under visible light was used as a model system. Before irradiation, the photocatalysts (2 mg) were dispersed in the mixture and stirred in the dark for 30 min to reach the adsorption–desorption equilibrium. Stirring was continued during the photocatalytic process. At the same time interval of 10 min, the reaction solution was taken out and transferred for UV analysis. The concentration of MB was monitored by measuring the absorption intensity at the maximum absorption wavelength of λ = 664.0 nm by a UV-vis spectrophotometer.

Table 1 Crystal data and structural refinement parameters for **MOF-1**

Compound	**MOF-1**
CCDC	1962617
Formula	$C_{57}H_{39}NNd_2O_{20}$
Crystal system	Triclinic
Space group	$P\bar{1}$
a/Å	5.4980(2)
b/Å	13.6342(6)
c/Å	18.1214(6)
α/°	72.607(3)
β/°	85.403(3)
γ/°	80.601(4)
V/Å^3	1278.18(9)
T/K	173
Z	1
R_{int}	0.030
GOF	1.05
F(000)	668
ρ_{calcd} (g cm^{-3})	1.749
μ, mm^{-1}	16.04
R_1/wR_2 ($I > 2\sigma(I)$)[a]	0.0309/0.0900
R_1/wR_2 (all data)[b]	0.0323/0.0915
$\rho_{max,min}$, e (e Å^{-3})	1.67/−0.67

[a] $R_1 = \sum||F_o| - |F_c||/\sum|F_o|$. [b] $wR^2 = [\sum w(F_o^2 - F_c^2)^2/\sum w(F_o^2)^2]^{1/2}$.

Results and discussion

Crystal structure of $[Nd_2(TCPB)_2(DMF)(H_2O)]_n$

$[Nd_2(TCPB)_2(DMF)(H_2O)]_n$ crystallizes in the $P\bar{1}$ space group of the triclinic. The asymmetric unit contains one Nd^{3+} cation, one $TCPB^{3-}$ ligand, a half coordinated DMF, and a half coordinated H_2O (Fig. 1a). Each Nd^{3+} ion coordinated with eight oxygen atoms from six independent $TCPB^{3-}$ ligands (O4, $O4^{v}$, $O5^{ii}$, $O6^{i}$, $O7^{iii}$, $O8^{iv}$, $O9^{iv}$), a half coordinated H_2O (O10) and a half coordinated DMF (O11), respectively, to show a distorted dodecahedron. The bond length of the Nd–O is in the range of 2.328(3)–2.646(3) Å (Table S1†). To better observe the three-dimensional network structure of **MOF-1**, the whole network can be regarded as a topologically connected framework with a point symbol of $(4^{11}\cdot6^4)$ from the TOPOS program analysis (Fig. 1b).

Characterization of MOF-1

To identify the phase purity of **MOF-1**, the PXRD spectra were recorded at room temperature. The PXRD pattern of $[Nd_2(TCPB)_2(DMF)(H_2O)]_n$ is consistent with its simulated pattern from the single crystal data, indicating the high purity of **MOF-1** (Fig. S1†). The thermal stability of **MOF-1** was carried out by thermogravimetric analysis (TGA) (Fig. S2†), and the result indicated that **MOF-1** could maintain the framework until about 530 °C.

Characterizations of MOF-1/GO/Fe_3O_4 composite

The PXRD patterns of the original GO, Fe_3O_4, **MOF-1**, and **MOF-1**/GO/Fe_3O_4 nanocomposites are shown in Fig. 2a. GO displayed an intense and sharp diffraction peak at about 2θ = 11.14°, and the corresponding interlayer spacing was obtained as 0.79 nm from Bragg's law.[29] In **MOF-1**/GO/Fe_3O_4 nano-

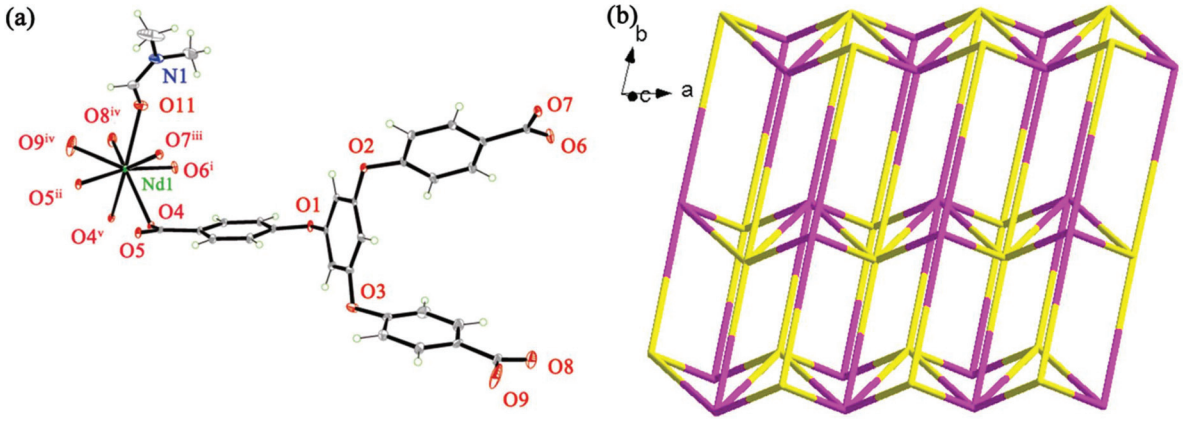

Fig. 1 (a) Coordination environment of Nd^{3+} cations and atomic labeling scheme in **MOF-1** (coordinated H_2O molecules are omitted for clarity). Symmetry codes: (i) $-x + 1, -y + 1, -z + 2$; (ii) $-x + 1, -y + 1, -z + 1$; (iii) $-x, -y + 1, -z + 2$; (iv) $x + 1, y + 1, z - 1$; (v) $-x + 2, -y + 1, -z + 1$; and (vi) $x - 1, y - 1, z + 1$. (b) Topological structure. The Nd units and the $tcpb^{3-}$ anions are shown in pink and yellow, respectively.

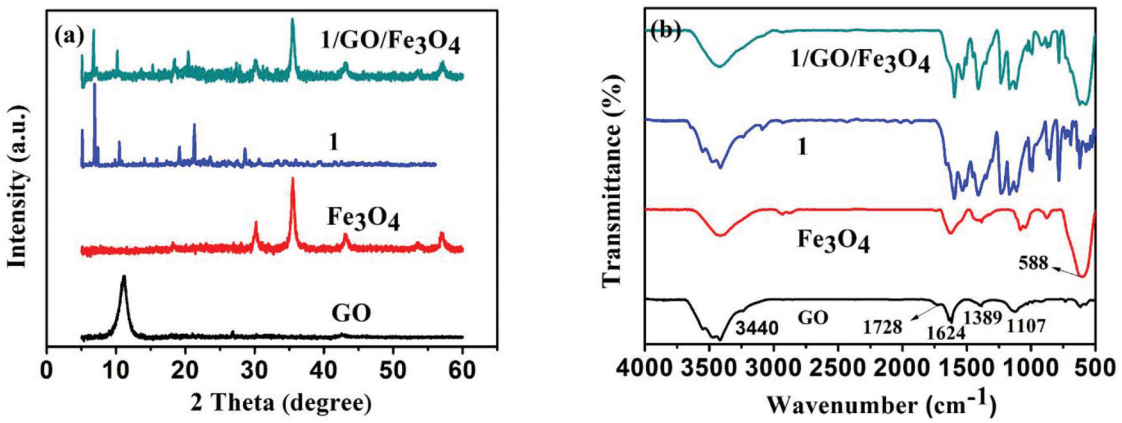

Fig. 2 The PXRD patterns (a) and FT-IR spectroscopy spectra (b) of GO, Fe_3O_4, **MOF-1**, and **MOF-1**/GO/Fe_3O_4.

composites, the main peaks of **MOF-1** were retained, indicating that the **MOF-1** structure was mainly maintained and the graphene layers of GO only caused slight distortions.[30] However, no obvious diffraction peaks of GO were observed in this ternary material because the relatively low content of GO in the sample made the peak weaker. This phenomenon is also similar to previous reports.[31] The characteristic diffraction peak of Fe_3O_4 could also be observed in Fig. 2a, which confirms the successful preparation of the **MOF-1**/GO/Fe_3O_4 nanocomposite.[32]

The FT-IR spectroscopy of GO, Fe_3O_4, **MOF-1**, and **MOF-1**/GO/Fe_3O_4 nanocomposites was performed as shown in Fig. 2b. The absorption band located at 588 cm^{-1} was assigned to the Fe–O vibration.[2,33] In the FT-IR spectrum of GO, the strong and broad band at around 3440 cm^{-1} is related to the hydroxyl stretching vibration (O–H) produced by –COOH group and H_2O molecule.[34] The absorption bands at 1728 cm^{-1} and 1624 cm^{-1} arise due to the C=O and C=C stretching vibrations, respectively.[35] Furthermore, the absorption bands at 1389 cm^{-1} and 1107 cm^{-1} can be attributed to the stretching vibrations of C–OH and C–O.[36] Therefore, a large number of oxygen-containing functional groups could be introduced into the GO nanosheets during the oxidation process. As shown in Fig. 2b, the characteristic absorption bands of **MOF-1** are dominant in **MOF-1**/GO/Fe_3O_4 composites. Compared with pure **MOF-1** nanocomposites, the strength and position of the bands of **MOF-1**/GO/Fe_3O_4 composites demonstrated no clear change, suggesting that the composition of the **MOF-1** unit is not inhibited by the graphene layers. The spectra of the **MOF-1**/GO/Fe_3O_4 nanocomposite also combined the features of the composites, and the characteristic absorption bands of each component are provided. This phenomenon supports the results of PXRD and indicates the existence of **MOF-1** and Fe_3O_4 in the composites.

The morphology of the synthesized **MOF-1**/GO and **MOF-1**/GO/Fe_3O_4 nanocomposites was characterized by SEM. The SEM image of **MOF-1**/GO nanocomposite (Fig. 3a and b) showed that the **MOF-1** nanoparticles and the GO sheets have been integrated by intimate interfacial contact.[37] As shown in Fig. 3c, **MOF-1**/GO/Fe_3O_4 had a large number of Fe_3O_4 micro-

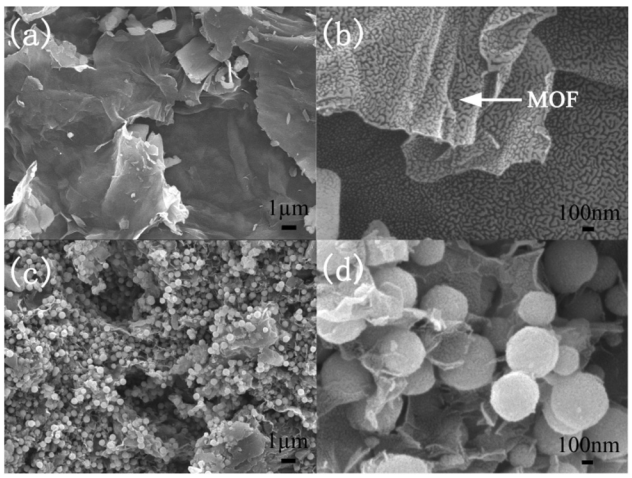

Fig. 3 SEM images of **MOF-1**/GO (a and b) and **MOF-1**/GO/Fe_3O_4 (c and d).

spheres with a diameter of about 400 nm that were loaded on the thin surface of GO, and the size of the magnetic microspheres was uniform, as reported previously.[28,33] As presented in Fig. 3d, in addition to loading lots of Fe_3O_4 microspheres on the surface of GO, a large amount of **MOF-1** nanoparticles were loaded.

Therefore, as demonstrated by the SEM results, the novel **MOF-1**/GO/Fe_3O_4 nanocomposite had been successfully prepared.

The N_2 adsorption–desorption isotherm of the as-synthesized photocatalysts was carried out at 77 K to investigate the specific surface area and the pore volume. As presented in Fig. S3,† the BET surface area of **MOF-1**/GO/Fe_3O_4 nanocomposite was calculated as 48.80 m^2 g^{-1}. The isotherms are representative type-IV isotherms according to the IUPAC classification, indicating that the resultant **MOF-1**/GO/Fe_3O_4 nanocomposite belongs to the mesoporous material. The improved surface area possibly arises due to the large number of micropores produced at the interface between the GO and **MOF-1** components,[30] as proved by the N_2 isotherm measured on the **MOF-1**/GO/Fe_3O_4 nanocomposite and the corresponding SEM images. Moreover, the comparatively high surface area could play a vital role in both improving the light absorption capability and providing enough high active sites for driving the photocatalytic reactions.[34,38]

The absorbance properties of **MOF-1**/GO/Fe_3O_4 nanocomposite and pure **MOF-1** were investigated *via* UV-Vis DRS. In the visible region, the absorption intensity of the heterostructure composite was noticeably higher than that of pure **MOF-1**, revealing that the addition of GO can improve the photocatalytic performance of **MOF-1**.[39–41] Also, the red shift of the absorption wavelength showed that these composites could absorb visible light, suggesting that they may be good photocatalysts for the photo-driven applications[42] (Fig. 4a). The bandgap energies can be calculated by the equation $\alpha h\nu = A(h\nu - E_g)^{n/2}$, where α, h, ν and A represent the absorption

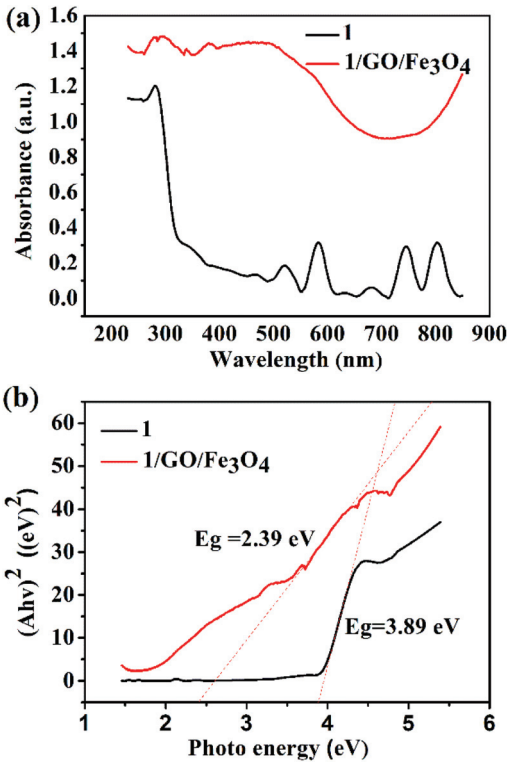

Fig. 4 UV–vis DRS (a) and the bandgaps (b) of the **MOF-1** and **MOF-1**/GO/Fe_3O_4 nanocomposites.

coefficient, the Planck's constant, the light frequency, and proportionality constant, respectively.[43] The n are 4 and 1 for the calculation of direct and indirect bandgaps of semiconductors, respectively, and E_g represents the absorption bandgap energy.[44,45] The optical bandgap energies of the **MOF-1** and **MOF-1**/GO/Fe_3O_4 nanocomposites were found to be 3.89 and 2.39 eV, respectively (Fig. 4b). Notably, the optical bandgap energy of the **MOF-1**/GO/Fe_3O_4 nanocomposite decreased due to the introduction of GO as compared with pure **MOF-1**. The results indicated that GO played a vital role in decreasing the optical bandgap, broadening visible light absorption range, and improving the utilization ratio of visible light, which is analogous to that reported in the literature.[46] Hence, the synthesized materials demonstrated excellent photocatalytic performance under visible light irradiation.

Photocatalytic properties

The photocatalytic property was evaluated by the degradation of MB, RhB, and MO under visible light irradiation. The results showed that the composited photocatalyst displayed good specific degradation of MB; so, we chose MB as the representation (Fig. S4†). Several controlled experiments were first carried out to ensure that the results acquired from the photocatalytic tests were consistent and not affected by hydrolysis or photolysis. Fig. 5a shows the variation of MB concentration (C/C_0) with reaction time under different experimental conditions. There was negligible degradation of MB in the

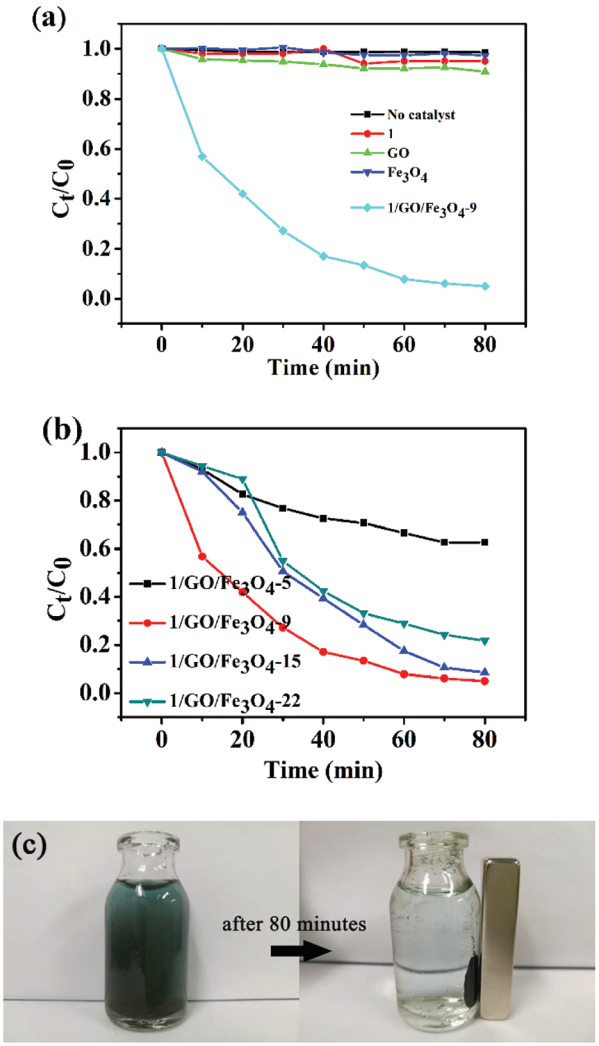

Fig. 5 Photocatalytic degradation of MB as a function of irradiation time for different photocatalysts: No catalyst, **MOF-1**, GO, Fe_3O_4, and **MOF-1**/GO/Fe_3O_4-9 (a). Photocatalytic degradation of MB as a function of irradiation time for a series of **MOF-1**/GO/Fe_3O_4-*x* photocatalysts (b). Photographic image of MB before and after degradation by **MOF-1**/GO/Fe_3O_4 and the recovery of the catalysts by applying an external magnet (c).

absence of catalysts under equivalent experimental conditions, suggesting that MB was quite stable towards incident light. Also, a blank experiment was performed wherein GO was used as a photocatalyst to degrade MB. It was noticeable that a negligible degradation of MB was detected in the presence of blank GO. Moreover, **MOF-1** and Fe_3O_4 had almost no degradation towards MB. However, after the composite was formed, there was a clear increase in the photocatalytic efficiency to up to 90%. This was because of the addition of GO which prevented the recombination of photogenerated electron–hole pairs and improved the photocatalytic performance. The photocatalytic activity of the composite was much better after the introduction of GO. It is crucial to control the addition ratio of GO for achieving optimal synergy interactions between GO and **MOF-1** for the photodegradation of MB under the same experimental conditions. As shown in Fig. 5b, the photocatalytic performance of the **MOF-1**/GO/Fe_3O_4 nanocomposite was extremely affected by the incorporation amount of GO. MB was primarily removed from the solution by the photodegradation of the **MOF**-1/GO/Fe_3O_4-5, 9, 15, 22 nanocomposites, and the photocatalytic percentage at 80 min was 57%, 95%, 91%, and 80%, respectively. The photocatalytic degradation efficiency increased with the increase in GO amount and reached the maximum when the content of GO was 9%. However, upon further increasing the loading amount of GO, the degradation ratio of MB in the aqueous solutions decreased, but was still higher than that of pure **MOF-1**. This phenomenon had also been reported in the literature.[47] Based on the experimental results, we concluded that 9% **MOF-1**/GO/Fe_3O_4 displayed a superb photocatalytic performance towards the photocatalytic degradation of MB. These results may be due to the fact that some active sites on the surface of **MOF-1** are hindered by the additional GO when the content of GO is high, resulting in reduced photocatalytic activity.[48] Notably, the 9% **MOF-1**/GO/Fe_3O_4 nanocomposite as an optimum sample achieved the highest final degradation (95%) of MB dye by the aid of photocatalysis, and MB was almost completely colorless after 80 min of visible light irradiation. The fundamental cause of this phenomenon is the introduction of GO that is conducive to the separation of electron–hole pairs. Moreover, the prepared **MOF-1**/GO/Fe_3O_4 photocatalyst could be recovered from the solution under an external magnetic field (Fig. 5c), directly demonstrating that the composites can be used as a convenient and recoverable photocatalyst in practical applications. Thus, we took 9% of GO in **MOF-1**/GO/Fe_3O_4 as a proper ratio for further research. The kinetic curve of MB degradation is generally considered to follow the pseudo-first-order linear transformation process $\ln(C_0/C) = kt$ (Fig. S5†) that is used to calculate the MB degradation rate over these four photocatalysts. The reaction rate constants over the **MOF-1**/GO/Fe_3O_4-9 nanocomposite were about 6.4, 1.1, and 1.8 times larger than that of **MOF-1**/GO/Fe_3O_4-5, 15, and 22 nanocomposites, respectively. The **MOF-1**/GO/Fe_3O_4-9 nanocomposite exhibited better degradation performance and a higher degradation rate constant for MB. Compared with the well-behaved photocatalysts in the recent works (Table S2†), the degradation performance of the **MOF-1**/GO/Fe_3O_4 nanocomposite was superior to most of the reported MOF-based hybrid nanocomposite photocatalysts.

To evaluate the feasibility of catalysts in practical applications, the stability and reusability of **MOF-1**/GO/Fe_3O_4 catalysts were investigated. In this work, the photocatalysts were recovered by ultrasound and washed with water and ethanol. The recovered sample was used in the next cycle, while all the other reaction conditions remained unchanged. It can be seen from Fig. 6a that the photocatalytic activity of the synthetic photocatalysts had no obvious alterations during four consecutive recycles for the degradation of MB, which suggested that the **MOF-1**/GO/Fe_3O_4 photocatalysts had high stability and can be used for repeated disposal of MB dyes. The reusability and

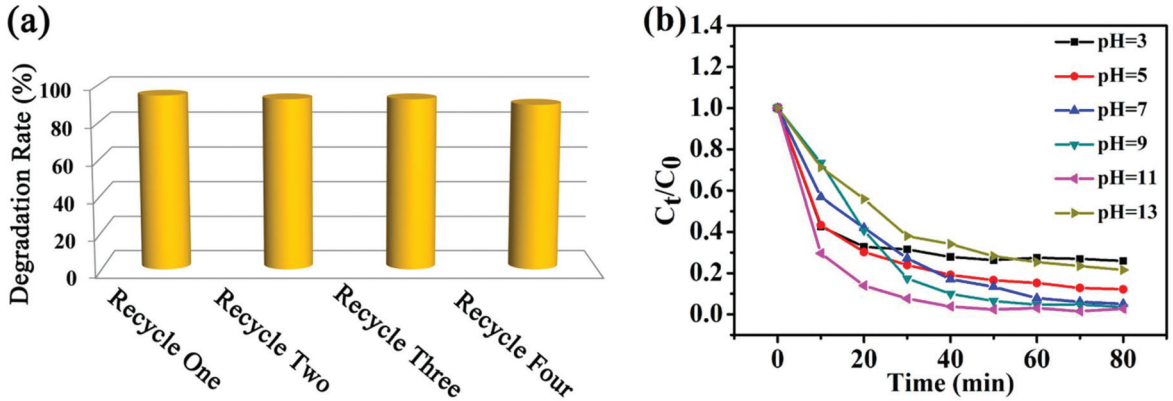

Fig. 6 The reusability of the **MOF-1**/GO/Fe_3O_4-9 nanocomposite for the degradation of MB (a). Effect of initial pH on the degradation of MB (b).

stability of these photocatalysts are more superior than most of the MOFs-based photocatalysts reported to date.[45] In addition, the PXRD (Fig. S6a†) and FT-IR (Fig. S6b†) data of the fresh and used photocatalysts revealed that the **MOF-1**/GO/Fe_3O_4 nanocomposite had no discernible modification even after four cycles of reaction, which verified the excellent stability of the **MOF-1**/GO/Fe_3O_4 nanocomposite as a photocatalyst. To confirm the practical utility of the composited photocatalyst, we performed the photocatalytic degradation experiment at different pH values. As shown in Fig. 6b, the catalyst demonstrated excellent stability, which displayed a high photocatalytic activity in the pH range of 5–11. When the catalysts contained GO, it overcame the sensitivity of the process to pH due to the high functional groups of GO, verifying that the **MOF-1**/GO/Fe_3O_4 photocatalyst can be efficiently used in a wide range of pH.[49] Besides, the number of iron ions leaching at low pH was measured by ICP (Table S3†). The ICP results demonstrate that the leaching of the iron ions at pH = 3 and 5 are 2.166 and 0.221 mg L^{-1}, respectively, almost 1.6% and 0.2% compared to the **MOF-1**/GO/Fe_3O_4 nanocomposite (133 mg L^{-1}). Therefore, the applicable conditions of the material should be in the pH range of 5–11.[50]

Possible photocatalytic mechanisms

To understand the mechanism of photodegradation, $AgNO_3$ (an e^- scavenger), EDTA-2Na (an h^+ scavenger), and *tert*-butanol (a $^{\bullet}OH$ scavenger) were used to trap e^-, h^+, and $^{\bullet}OH$ to detect major active species in the photocatalytic process (Fig. 7a).[51] The addition of *tert*-butanol had no significant effects on the photocatalytic degradation, demonstrating that $^{\bullet}OH$ was not the reactive oxidation species in this reaction. In contrast, the evidently inhibitory effects of $AgNO_3$ and EDTA-2Na manifested that the photogenerated electron and h^+ played key roles in the photocatalytic degradation of MB.

To get deeper insights into the photoinduced charge separation and transfer properties, the electrochemical impedance spectroscopy (EIS) analysis was implemented.[20] The results are depicted in Fig. 7b; the **MOF-1**/GO/Fe_3O_4 nanocomposite has a smaller radius of curvature as compared to pure **MOF-1**, demonstrating the most efficient charge separation over the **MOF-1**/GO/Fe_3O_4 nanocomposite.[52,53] Therefore, the photoelectric properties analyzed earlier obviously indicate that the doping with GO and Fe_3O_4 is an efficient approach for improving the light-harvesting ability and charge separation

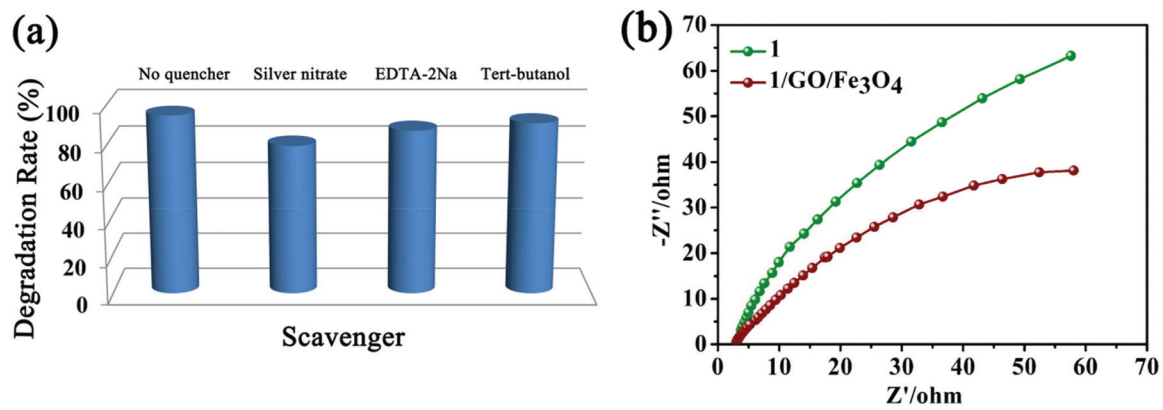

Fig. 7 Effect of different scavengers on the photodegradation of MB by **MOF-1**/GO/Fe_3O_4-9 nanocomposite under visible-light irradiation (a). EIS Nyquist plots of **MOF-1**/GO/Fe_3O_4-9 and **MOF-1** (b).

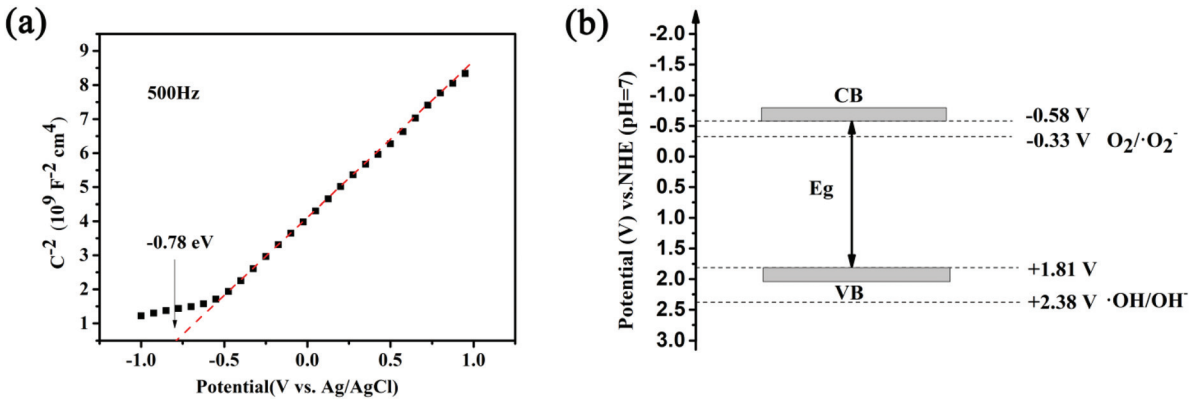

Fig. 8 Mott–Schottky plots (a) and estimated energy level diagram (b) of the **MOF-1**/GO/Fe_3O_4.

efficiency, which is beneficial to improve the photocatalytic activity.

Also, liquid chromatography-mass spectrometry (LC-MS) is an effective method to further identify the mechanism of the photocatalytic degradation reaction.[54] As shown in Fig. S7,† the initial concentration of MB after catalytic degradation under visible light decreased with retention time at 6.22 min. The peak of mass spectrometry was primarily caused by the 284 *m*/*z* fragment, which is identified as the molecular ion peak of MB, indicating the degradation of MB. There is a sharp peak at 1.13 min in the liquid chromatography data of MB aqueous solution after the degradation, which is similar to the liquid chromatography data of distilled water at 1.15 min. It may be attributed to some components in the distilled water. No other peaks were observed, indicating that there was no stable production of active intermediates in the photocatalytic degradation process.

In addition, the Mott–Schottky measurements were performed to study the enhanced photocatalytic mechanism of MB degradation by **MOF-1**/GO/Fe_3O_4. As shown in Fig. 8a, the positive slope of the straight line indicates that **MOF-1**/GO/Fe_3O_4 is an n-type semiconductor and its conduction band potential (E_{CB}) is very close to the flat-band potential (E_{FB}). Therefore, the conduction band potential (E_{CB}) of the **MOF-1**/GO/Fe_3O_4 nanocomposites is extrapolated to about −0.78 V *vs.* Ag/AgCl (−0.58 V *vs.* NHE),[55] which is lower than $O_2/{}^{\bullet}O_2^-$ potential (−0.33 V *vs.* NHE),[56] demonstrating that the photogenerated electrons on the CB of the **MOF-1**/GO/Fe_3O_4 nanocomposites are conducive to the reduction of O_2 (Fig. 8b). Combined with the bandgap energy calculated by the UV-vis DRS spectra, the valence band potential (E_{VB}) of the **MOF-1**/GO/Fe_3O_4 nanocomposites is calculated to be 1.61 V *vs.* Ag/AgCl (1.81 V *vs.* NHE), which is lower than the redox potential of ${}^{\bullet}OH/OH^-$ (2.38 V *vs.* NHE), indicating that the **MOF-1**/GO/Fe_3O_4 nanocomposites cannot generate ${}^{\bullet}OH$ radicals by oxidizing OH^- through h^+, but directly oxidize MB. That is why ${}^{\bullet}OH$ has a negligible effect on the photocatalytic performance.

Combined with the above results, a tentative mechanism of the semiconductor theory of the photocatalytic degradation of MB over **MOF-1**/GO/Fe_3O_4 nanocomposites was proposed.[57] In the process of photocatalysis, the interaction between the photocatalyst and organic dyes was the key factor to improve the performance of the photocatalytic degradation of organic dyes, which usually occurred on the surface of the photocatalyst. The **MOF-1**/GO/Fe_3O_4 nanocomposites were excited and then the photogenerated electrons/holes were created under visible-light irradiation. The photogenerated holes with a strong oxidation capacity can directly oxidize MB. Meanwhile, the photogenerated electrons were captured by the GO, which hindered the efficient recombination of photogenerated electron–hole pairs.[34,56,58] Moreover, the unique 2D structure of GO sheets made the photocatalytic reactions to occur on the GO sheets and on the surface of **MOF-1**/GO/Fe_3O_4 nanocomposites; thus, increasing the active sites and providing more catalytic centers. Consequently, the **MOF-1**/GO/Fe_3O_4 nanocomposites showed great photocatalytic activities in the photocatalytic redox reactions.

$$\textbf{MOF-1}/GO/Fe_3O_4 + hv \rightarrow \textbf{MOF-1}/GO/Fe_3O_4\ (h^+ + e^-) \quad (1)$$

$$\textbf{MOF-1}/GO/Fe_3O_4\ (e^-) + GO \rightarrow \textbf{MOF-1}/GO/Fe_3O_4 + GO\ (e^-) \quad (2)$$

$$GO\ (e^-) + O_2 \rightarrow {}^{\bullet}O_2^- + GO \quad (3)$$

$${}^{\bullet}O_2^- + MB \rightarrow \text{other products} \rightarrow CO_2 + H_2O \quad (4)$$

$$h^+ + MB \rightarrow \text{other products} \rightarrow CO_2 + H_2O \quad (5)$$

Conclusions

We synthesized a novel composite photocatalyst **MOF-1**/GO/Fe_3O_4 for efficient MB degradation in aqueous solutions. It is the first photocatalyst based on the Nd-MOF for degradation. The photocatalytic performance of the **MOF-1**/GO/Fe_3O_4 nanocomposites was up to 95% for the degradation of MB within 80 min under sunlight irradiation without any other reagents, which is better than that of pure **MOF-1** nanocomposites. The

introduction of GO hindered the recombination of photogenerated electron–hole pairs and improved the optical absorption properties of the **MOF-1**/GO/Fe_3O_4 nanocomposites. Moreover, the ternary composite demonstrated excellent stability over a wide pH range. The performance of **MOF-1**/GO/Fe_3O_4 nanocomposites for MB degradation presented in this work is the best among the reported hybrid nanocomposite photocatalysts based on MOFs. Furthermore, the **MOF-1**/GO/Fe_3O_4 nanocomposites could be easily recovered and reused from the treated water through an external magnetic field, suggesting low operating costs compared with traditional wastewater treatment technology. This study opens up a new route to design and synthesize new-style, visible light active photocatalysts for wastewater treatment containing organic dyes in environmental applications.

Conflicts of interest

There are no conflicts to declare.

Acknowledgements

This work was supported by the Natural Science Foundation of China (Grant No 21671124); the Natural Science Foundation of Shanxi Province (201701D121039); the Fund for Shanxi "1331 Project" Key Innovative Research Team (1331KIRT); and the Undergraduate Research Training Plan Project of the Shanxi University. A portion of this work was performed on the Scientific Instrument Center of the Shanxi University of China.

Notes and references

1 C. Ma, Z. Yang, W. Wang, M. Zhang, X. Hao, S. Zhu and S. Chen, *J. Mater. Chem. C*, 2020, **8**, 2888–2898.
2 S. Banerjee, P. Benjwal, M. Singh and K. K. Kar, *Appl. Surf. Sci.*, 2018, **439**, 560–568.
3 P. K. Boruah, P. Borthakur, G. Darabdhara, C. K. Kamaja, I. Karbhal, M. V. Shelke, P. Phukan, D. Saikia and M. R. Das, *RSC Adv.*, 2016, **6**, 11049–11063.
4 C. Feng, Z. Chen, J. Jing and J. Hou, *J. Mater. Chem. C*, 2020, **8**, 3000–3009.
5 D. Sun, Y. Fu, W. Liu, L. Ye, D. Wang, L. Yang, X. Fu and Z. Li, *Chem. – Eur. J.*, 2013, **19**, 14279–14285.
6 Q. Wang, Q. Gao, A. M. Al-Enizi, A. Nafady and S. Ma, *Inorg. Chem. Front.*, 2020, **7**, 300–339.
7 L. Shi, T. Wang, H. Zhang, K. Chang, X. Meng, H. Liu and J. Ye, *Adv. Sci.*, 2015, **2**, 1500006.
8 M. Alvaro, E. Carbonell, B. Ferrer, F. X. Llabres i Xamena and H. Garcia, *Chemistry*, 2007, **13**, 5106–5112.
9 J. Wang, J. Wan, Y. Ma, Y. Wang, M. Pu and Z. Guan, *RSC Adv.*, 2016, **6**, 112502–112511.
10 Y. Li, G. Hou, J. Yang, J. Xie, X. Yuan, H. Yang and M. Wang, *RSC Adv.*, 2016, **6**, 16395–16403.
11 X. P. Wu, L. Gagliardi and D. G. Truhlar, *J. Am. Chem. Soc.*, 2018, **140**, 7904–7912.
12 Q. Yang, Q. Xu and H. L. Jiang, *Chem. Soc. Rev.*, 2017, **46**, 4774–4808.
13 J. D. Xiao and H. L. Jiang, *Acc. Chem. Res.*, 2019, **52**, 356–366.
14 S. Liu, C. Liu, W. Wang, B. Cheng and J. Yu, *Nanoscale*, 2012, **4**, 3193–3200.
15 D. Xu, B. Cheng, S. Cao and J. Yu, *Appl.Catal.,B*, 2015, **164**, 380–388.
16 C. Petit and T. J. Bandosz, *Adv.Funct.Mater.*, 2011, **21**, 2108–2117.
17 C. Petit and T. J. Bandosz, *Adv. Mater.*, 2009, **21**, 4753–4757.
18 K. Yang, Y. Yan, H. Wang, Z. Sun, W. Chen, H. Kang, Y. Han, W. Zahng, X. Sun and Z. Li, *Nanoscale*, 2018, **10**, 17647–17655.
19 J. Cai, J.-Y. Lu, Q.-Y. Chen, L.-L. Qu, Y.-Q. Lu and G.-F. Gao, *New J. Chem.*, 2017, **41**, 3882–3886.
20 P. Karthik, R. Vinoth, P. Zhang, W. Choi, E. Balaraman and B. Neppolian, *ACS Appl. Energy Mater.*, 2018, **1**, 1913–1923.
21 T. Peik-See, A. Pandikumar, L. H. Ngee, H. N. Ming and C. C. Hua, *Catal. Sci. Technol.*, 2014, **4**, 4396–4405.
22 C.-F. Zhang, L.-G. Qiu, F. Ke, Y.-J. Zhu, Y.-P. Yuan, G.-S. Xu and X. Jiang, *J. Mater. Chem. A*, 2013, **1**, 14329.
23 J. Zheng, Z. Lin, G. Lin, H. Yang and L. Zhang, *J. Mater. Chem. B*, 2015, **3**, 2185–2191.
24 W. Guan, X. Gao, G. Ji, Y. Xing, C. Du and Z. Liu, *J. Solid State Chem.*, 2017, **255**, 150–156.
25 X. Ke, X. Song, N. Qin, Y. Cai and F. Ke, *J. Porous Mater.*, 2018, **26**, 813–818.
26 F. Wang, Y. Zhou, X. Pan, B. Lu, J. Huang and Z. Ye, *Phys. Chem. Chem. Phys.*, 2018, **20**, 6959–6969.
27 G. M. Sheldrick, *ActaCrystallogr., Sect. C:Struct.Chem.*, 2015, **71**, 3–8.
28 H. Deng, X. Li, Q. Peng, X. Wang, J. Chen and Y. Li, *Angew. Chem., Int. Ed.*, 2005, **44**, 2782–2785.
29 C. Petit, J. Burress and T. J. Bandosz, *Carbon*, 2011, **49**, 563–572.
30 Y. Chen, D. Lv, J. Wu, J. Xiao, H. Xi, Q. Xia and Z. Li, *Chem. Eng. J.*, 2017, **308**, 1065–1072.
31 X. Qiu, X. Wang and Y. Li, *Chem. Commun.*, 2015, **51**, 3874–3877.
32 S. Zhang, Y. Wang, Z. Cao, J. Xu, J. Hu, Y. Huang, C. Cui, H. Liu and H. Wang, *Chem. Eng. J.*, 2020, **381**, 122771.
33 J. Ni, J. Xue, L. Xie, J. Shen, G. He and H. Chen, *Phys. Chem. Chem. Phys.*, 2017, **20**, 414–421.
34 X. Li, Z. Le, X. Chen, Z. Li, W. Wang, X. Liu, A. Wu, P. Xu and D. Zhang, *Appl.Catal.,B*, 2018, **236**, 501–508.
35 N. M. Mahmoodi, M. Oveisi and E. Asadi, *J. Cleaner Prod.*, 2019, **211**, 198–212.
36 M. Y. Miao, J. T. Feng, Q. Jin, Y. F. He, Y. N. Liu, Y. Y. Du, N. Zhang and D. Q. Li, *RSC Adv.*, 2015, **5**, 36066–36074.
37 Y. Liu, M. Zhu, M. Chen, L. Ma, B. Yang, L. Li and W. Tu, *Chem. Eng. J.*, 2019, **359**, 47–45.
38 H. Jia, D. Ma, S. Zhong, L. Li, L. Li, L. Xu and B. Li, *Chem. Eng. J.*, 2019, **368**, 165–174.

39 Y. Bu, Z. Chen, W. Li and B. Hou, *ACS Appl. Mater. Interfaces*, 2013, **5**, 12361–12368.
40 Y. Zhang, G. Li, H. Lu, Q. Lv and Z. Sun, *RSC Adv.*, 2014, **4**, 7594.
41 Y. Zheng, X. Hou, Q. Li, Z. Fang, T. Yang, T. Liang, X. Duan, M. Shang and W. Yang, *J. Mater. Chem. C*, 2020, **8**, 1803–1810.
42 K. Hu, R. Li, C. Ye, A. Wang, W. Wei, D. Hu, R. Qiu and K. Yan, *J. Cleaner Prod.*, 2020, **253**, 120055.
43 X. J. Chen, Y. Z. Dai, X. Y. Wang, J. Guo, T. H. Liu and F. F. Li, *J. Hazard. Mater.*, 2015, **292**, 9–18.
44 X. Zou, Y. Dong, X. Zhang and Y. Cui, *Appl. Surf. Sci.*, 2016, **366**, 173–180.
45 X. Li, Y. Pi, L. Wu, Q. Xia, J. Wu, Z. Li and J. Xiao, *Appl. Catal.,B*, 2017, **202**, 653–663.
46 C. Yang, X. You, J. Cheng, H. Zheng and Y. Chen, *Appl. Catal.,B*, 2017, **200**, 673–680.
47 N. Liu, W. Huang, X. Zhang, L. Tang, L. Wang, Y. Wang and M. Wu, *Appl.Catal.,B*, 2018, **221**, 119–128.
48 L. Huang and B. Liu, *RSC Adv.*, 2016, **6**, 17873–17879.
49 Z. Jiang, L. Wang, J. Lei, Y. Liu and J. Zhang, *Appl.Catal.,B*, 2019, **241**, 367–374.
50 R. Liang, L. Shen, F. Jing, N. Qin and L. Wu, *ACS Appl. Mater. Interfaces*, 2015, **7**, 9507–9515.
51 L.-Q. Zuo, T.-F. Zhang, Z.-K. Zhang, J.-X. Hou, G.-J. Liu, J.-L. Du and L.-J. Li, *Inorg. Chem. Commun.*, 2019, **99**, 113–118.
52 Y. Zuo, J. Chen, H. Yang, M. Zhang, Y. Wang, G. He and Z. Sun, *J. Mater. Chem. C*, 2019, **7**, 9065–9074.
53 J. D. Xiao, Q. Shang, Y. Xiong, Q. Zhang, Y. Luo, S. H. Yu and H. L. Jiang, *Angew. Chem., Int. Ed.*, 2016, **55**, 9389–9393.
54 S. Feng, F. Jia, L. Lu, Z. Li and S. Zhang, *Chem. Commun.*, 2016, **52**, 4294–4297.
55 R. Liang, S. Luo, F. Jing, L. Shen, N. Qin and L. Wu, *Appl. Catal.,B*, 2015, **176–177**, 240–248.
56 D. Yu, L. Li, M. Wu and J. C. Crittenden, *Appl.Catal.,B*, 2019, **251**, 66–75.
57 F.-N. Shi, M. Lu, Y.-W. Bai, F. Liang, X.-Y. Song, G. Xu, X.-Q. Fan, X.-H. Yu, H.-P. You and Z. Zhao, *Cryst. Growth Des.*, 2018, **18**, 5045–5053.
58 Z. Yang, X. Xu, X. Liang, C. Lei, Y. Wei, P. He, B. Lv, H. Ma and Z. Lei, *Appl.Catal.,B*, 2016, **198**, 112–123.